

1           **The Stability-number as new metric for electrocatalyst stability benchmarking –**

2  
3  
4 Simon Geiger<sup>a,†,\*</sup>, Olga Kasian<sup>a,†</sup>, Marc Ledendecker<sup>a</sup>, Enrico Pizzutilo<sup>a</sup>, Andrea M. Mingers<sup>a</sup>,  
5       Wen Tian Fu<sup>b</sup>, Oscar Diaz-Morales<sup>b</sup>, Zhizhong Li<sup>c</sup>, Tobias Oellers<sup>d</sup>, Luc Fruchter<sup>c</sup>, Alfred  
6       Ludwig<sup>d</sup>, Karl J. J. Mayrhofer<sup>a,e,f</sup>, Marc T. M. Koper<sup>b</sup>, Serhiy Cherevko<sup>a,e,\*</sup>

7  
8                   <sup>a</sup> *Department of Interface Chemistry and Surface Engineering,*

9                   *Max-Planck-Institut für Eisenforschung GmbH, 40237 Düsseldorf, Germany*

10                  <sup>b</sup> *Leiden Institute of Chemistry, Leiden University, Leiden 2300 RA, The Netherlands.*

11                  <sup>c</sup> *Laboratoire de Physique des Solides, C.N.R.S., Université Paris-Sud, 91405 Orsay, France*

12                  <sup>d</sup> *Institute for Materials, Ruhr-Universität Bochum, 44801 Bochum, Germany*

13                  <sup>e</sup> *Helmholtz-Institute Erlangen-Nürnberg for Renewable Energy (IEK-11),*

14                               *Forschungszentrum Jülich, 91058 Erlangen, Germany*

15                  <sup>f</sup> *Department of Chemical and Biological Engineering, Friedrich-Alexander-Universität*

16                               *Erlangen-Nürnberg, 91058 Erlangen, Germany*

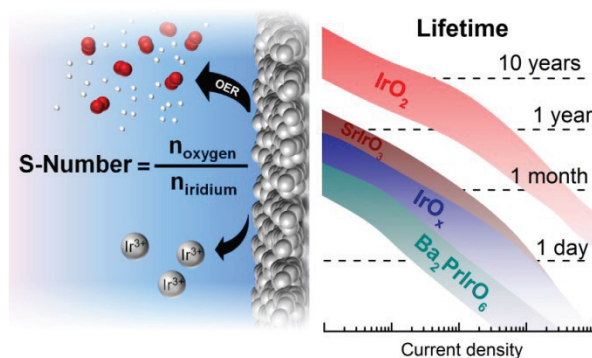
17  
18                   <sup>\*</sup> *Corresponding authors: geiger@mpie.de, s.cherevko@fz-juelich.de*

19                   <sup>†</sup> *These authors contributed equally to this work*

## 30 Abstract

31 Reducing noble metal loading and increasing specific activity of oxygen evolution catalysts  
32 are omnipresent challenges in proton exchange membrane (PEM) water electrolysis, which  
33 have recently been tackled by utilizing mixed oxides of noble and non-noble elements (e.g.  
34 perovskites, IrNiO<sub>x</sub>, etc.). However, proper verification of the stability of these materials is  
35 still pending. In this work dissolution processes of various iridium-based oxides are explored  
36 by introducing a new metric, defined as the ratio between amount of evolved oxygen and  
37 dissolved iridium. The so called Stability-number is independent of loading, surface area or  
38 involved active sites and thus, provides a reasonable comparison of diverse materials with  
39 respect to stability. Furthermore it can support the clarification of dissolution mechanisms and  
40 the estimation of a catalyst's lifetime. The case study on iridium-based perovskites shows that  
41 leaching of the non-noble elements in mixed oxides leads to formation of highly active  
42 amorphous iridium oxide, the instability of which is explained by participation of activated  
43 oxygen atoms, generating short-lived vacancies that favour dissolution. These insights are  
44 considered to guide further research which should be devoted to increasing utilization of pure  
45 crystalline iridium oxide, as it is the only known structure that guarantees a high durability in  
46 acidic conditions. In case amorphous iridium oxides are used, solutions for stabilization are  
47 needed.

48



49

50

Graphical abstract

51

52 **Keywords:** oxygen evolution reaction, iridium, perovskites, stability-number, energy  
53 conversion

54

## 55 1. Introduction

56 Electrochemical water splitting is considered to play a key role in the new energy scenario  
57 for the production of hydrogen, which can act as central energy carrier and as raw material for  
58 the chemical industry. Still, the persistent challenges of this concept are (i) slow kinetics of  
59 the oxygen evolution reaction (OER) and (ii) need of expensive materials as catalysts or  
60 related components. Especially for proton exchange membrane (PEM) electrolysis, the acidic  
61 environment caused by the membrane itself together with high anodic potentials limits the  
62 choice of catalyst materials to expensive noble metals. The best known catalysts for OER  
63 contain high amounts of scarce iridium that hampers large scale implementation of this  
64 technology. Smart catalyst design is needed to decrease noble metal loadings and increase  
65 specific activity and stability.

66 Various iridium-based mixed oxides<sup>1-8</sup> have been investigated as potential catalyst  
67 material to tackle the mentioned challenges by increased specific activity and lower  
68 percentage of expensive noble metals. Enhanced activity and apparently decent stability was  
69 demonstrated in comparison to IrO<sub>2</sub>, Ir-black, or other benchmark materials. However, the  
70 stability aspect needs more rigorous investigation. Especially non noble alkali or rare earth  
71 elements are expected to be thermodynamically unstable in acidic electrolytes,<sup>9</sup> favouring the  
72 formation of amorphous iridium oxide structures after leaching. The latter have been shown to  
73 degrade significantly in acidic electrolyte during OER,<sup>10-13</sup> accentuating the need for further  
74 understanding of degradation processes.

75 Most prominent examples are iridium-based perovskites recently investigated in acidic  
76 electrolyte.<sup>1,2</sup> Initial studies on the usage of this material class in electrocatalysis originate  
77 from Bockris and Otagawa,<sup>14,15</sup> who used alkaline electrolytes. Since then numerous studies  
78 on the usage of perovskites for alkaline water splitting have been published.<sup>16-25</sup> Exceptionally  
79 high OER activities were achieved for example by varying the occupancy of 3d orbitals of  
80 surface transition metals<sup>18</sup> or tuning oxygen vacancies by means of straining.<sup>21</sup> However,  
81 several groups brought up the important aspect of surface amorphization during OER.<sup>26-29</sup>  
82 May *et al.*<sup>26</sup> indicated, that especially those materials with high amorphization are the ones  
83 that show high activity, expressing the need of further investigations on the number of  
84 involved active sites. Even more in acid environment catalyst stability and amorphization is  
85 an issue. Therefore a thorough investigation of specific activity and dissolution processes of  
86 iridium-based perovskites in 0.1 M HClO<sub>4</sub> is presented in this work.

87 In general, contemporary challenges to explore new electrocatalysts are, in addition to  
88 increased activity: (i) the determination of the real electrochemical surface area (ECSA) by  
89 identification and quantification of the active sites enabling a reliable comparison of different  
90 materials and (ii) the investigation of degradation by thorough quantification of dissolution  
91 products, assuming the latter as major degradation process of electrocatalysts. Both  
92 parameters are important indicators of an electrocatalyst's performance. Our study aims to  
93 clear these important gaps by cyclic voltammetry to quantify active centres for OER and in  
94 situ dissolution data obtained by combining a scanning flow cell (SFC) with inductively  
95 coupled plasma mass spectrometry (ICP-MS). The amount of dissolved iridium is presented  
96 in relation to the evolved oxygen as new independent metric called Stability-number. The  
97 latter is beneficial to estimate lifetimes and together with online electrochemical mass  
98 spectrometry (OLEMS) underlines proposed dissolution mechanisms of the investigated  
99 materials, namely double perovskite powders with  $A_2B\text{IrO}_6$  structure ( $A = \text{Ba, Sr; B} = \text{Nd, Pr,}$   
100  $\text{Y}$ ), amorphous  $\text{IrO}_x$  powder, crystalline  $\text{IrO}_2$  powder,  $\text{SrIrO}_3$  perovskite films,  
101 electrochemically formed hydrous  $\text{IrO}_x$  films and crystalline  $\text{IrO}_2$  films. A general perspective  
102 on the applicability of the mentioned iridium oxide structures towards acidic water splitting is  
103 presented.

104

## 105 **2. Results and discussion**

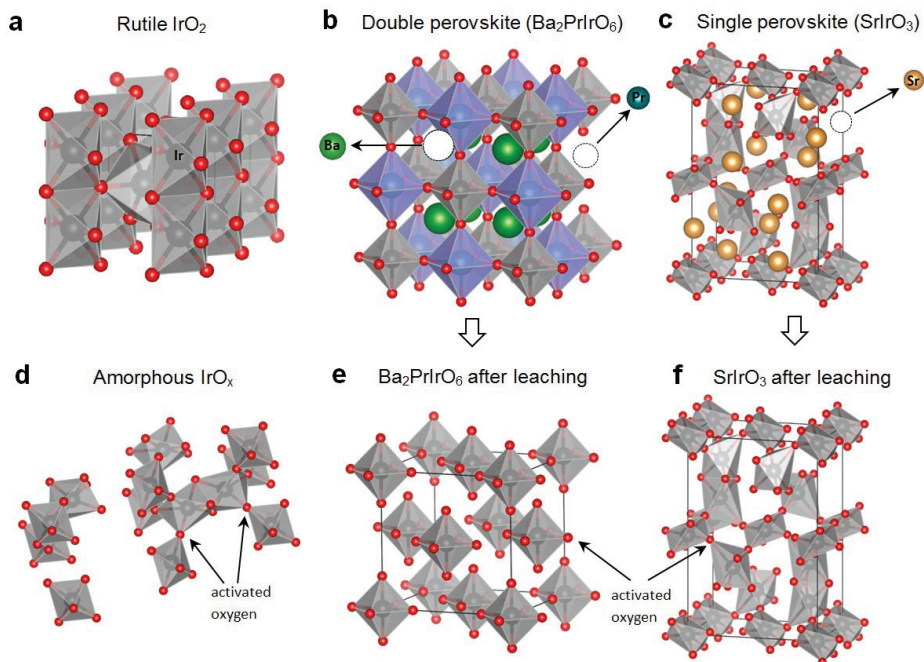
### 106 **Leaching processes in perovskites**

107 The catalyst composition on the surface is essential for exploring electrochemical  
108 reactions at the catalyst-electrolyte interface. Therefore, the dissolution behaviour of all  
109 materials was investigated during initial contact with 0.1 M  $\text{HClO}_4$  at open circuit potential  
110 (OCP). While crystalline  $\text{IrO}_2$  and amorphous  $\text{IrO}_x$  do not dissolve initially, perovskites do  
111 undergo intensive leaching. First of all the non-noble elements ( $\text{Ba, Sr, Nd, Pr, and Y}$ )  
112 dissolve as expected from available thermodynamic data<sup>9</sup> for single elements and related  
113 experimental works<sup>1,2</sup> (see Tab. S1 and Fig. S1, S3). However, in double-perovskites we  
114 observed dissolution of iridium as well in the range of 30-40 w% from the initial value,  
115 during 60 s of contact at OCP. This can be explained on the basis of the crystal structure  
116 illustrated in Fig. 1b. As the component B (e.g. Pr) is part of the lattice, leaching of the latter  
117 goes hand in hand with generation of isolated  $\text{IrO}_6$  octahedra, which are prone to dissolve in  
118 parallel. Furthermore we expect that the structure will collapse and reform in an amorphous  
119 iridium oxide. To underline this statement one exemplary material of the double perovskite

120 family was examined during a prolonged leaching experiment. EDS analysis confirms  
121 complete removal of Ba and Pr after keeping the powder for 14 days in 0.1 M HClO<sub>4</sub>, leaving  
122 behind an amorphous iridium oxide structure, demonstrated by selected area electron  
123 diffraction (SAED) (see Fig. S2). The penetration depths of these methods are expected to be  
124 higher than the diameter of the investigated particle, hence, leaching and formation of  
125 amorphous iridium oxide is not restricted to the surface.

126 Single perovskites on the other hand consist of a coherent iridium oxide structure with  
127 intercalated non-noble elements (see Fig. 1c). Thus, initial dissolution of a 20 nm SrIrO<sub>3</sub> film  
128 is restricted to Sr (3.0 w%), while iridium oxide is fairly stable (0.01 w%) (see Fig. S3). The  
129 leftover backbone of iridium oxide equals an anatase structure.<sup>1,30</sup> However, no stable anatase  
130 phase of iridium oxide has been reported to the best of our knowledge. It is therefore highly  
131 probable that the structure will collapse as well into amorphous iridium oxide. Similar CV  
132 shapes of electrochemically grown hydrous IrO<sub>x</sub> and leached SrIrO<sub>3</sub> presented in Fig. 4d  
133 supports this assumption. Based on the obtained dissolution data and simple calculation,  
134 initial contact of SrIrO<sub>3</sub> with acid forms a 0.6 nm layer of hydrous iridium oxide, which  
135 increases in thickness during prolonged OER measurements (see Fig. S3).

136



137  
138 **Figure 1. Crystal structure of the investigated materials.** (a) rutile IrO<sub>2</sub>; (b) double perovskite (e.g.  
139 Ba<sub>2</sub>PrIrO<sub>6</sub>); (c) single perovskite (SrIrO<sub>3</sub>); (d) assumed structure of amorphous iridium oxide, gaps are filled  
140 with intercalated water molecules (not shown); (e) leached double perovskite showing isolated IrO<sub>6</sub> octahedra,  
141 which will collapse into an amorphous structure; (f) leached SrIrO<sub>3</sub> resulting in an “anatase” iridium oxide  
142 structure.

## 143 **The oxide structure and its relevance for activity and dissolution**

144 In order to understand the observed results on activity and stability presented later in  
145 the manuscript we continue with a discussion on oxide structures and oxidation states before  
146 and after the initial leaching process. In Fig. 1 the structures of rutile  $\text{IrO}_2$ , amorphous  $\text{IrO}_x$ , a  
147 double perovskite ( $\text{Ba}_2\text{PrIrO}_6$ ), and a single perovskite ( $\text{SrIrO}_3$ ) are presented. The dense  
148 packing and edge sharing oxygen of the octahedra in the rutile structure are in contrast to  
149 loose packing and corner sharing octahedra in  $\text{Ba}_2\text{PrIrO}_6$  and  $\text{SrIrO}_3$  generating lower  
150 coordinated oxygen atoms (activated oxygen). Leaching of the non-noble elements A and B in  
151  $\text{A}_2\text{BIrO}_6$  destroys the crystal structure of the double perovskite and pure octahedral elements  
152 are linked together randomly inducing a high number of accessible “activated oxygen atoms”  
153 and vacancies. Similar structures can be achieved by leaching Sr from  $\text{SrIrO}_3$  or Ni from  
154  $\text{IrNiO}_x$ .<sup>3,4</sup> Moreover, classical potential cycling of iridium metal<sup>31</sup> or mild calcination of  
155 iridium precursors<sup>11,32</sup> are optional preparation methods.

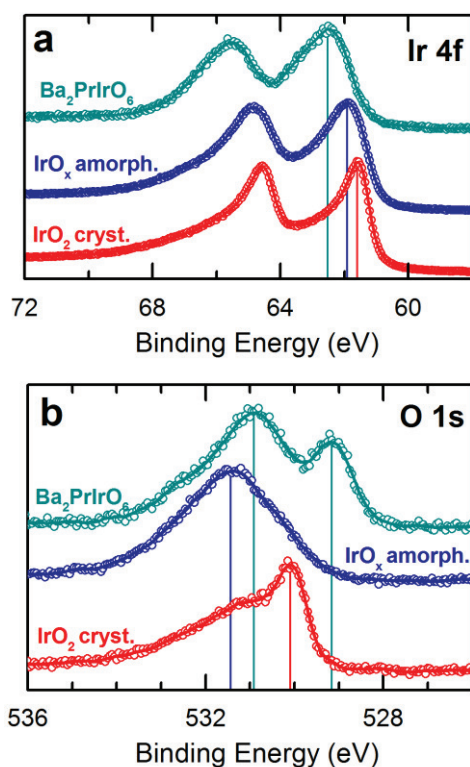
156 The binding energies of the 4f electrons of iridium and 1s electrons of oxygen  
157 obtained via X-ray photoemission spectroscopy (XPS) are utilized for further analysis on the  
158 chemical environment of iridium and oxygen in the structure. Based on a computational  
159 model, Pfeifer *et al.*<sup>33</sup> studied the formation of an iridium vacancy in a supercell. According to  
160 the calculations, this leads to the formation of  $\text{O}^{\cdot-}$  and  $\text{Ir}^{\text{III}}$  species, which was supported by  
161 XPS and NEXAFS investigations. Hereby, the authors explained the positive shift of the Ir 4f  
162 binding energy<sup>33</sup> in amorphous  $\text{IrO}_x$ , which is shown in Fig. 2a. The Ir 4f peak of  $\text{Ba}_2\text{PrIrO}_6$  is  
163 shifted to even higher binding energies, however, the pristine structure rather indicates the  
164 presence of  $\text{Ir}^{\text{V}}$ , which has a similar peak shift.<sup>34</sup> Still, Fu *et al.*<sup>35</sup> found a  $\text{Pr}^{\text{IV}}/\text{Ir}^{\text{IV}}$  couple  
165 present in  $\text{Ba}_2\text{PrIrO}_6$ , which is against the previous assumption. Consequently, based on XPS  
166 data solely, a clear statement on the oxidation states cannot be made. However, XPS clearly  
167 expresses the different environment of the iridium atoms in the respective structures. After  
168 leaching of  $\text{Ba}_2\text{PrIrO}_6$  in 0.1 M  $\text{HClO}_4$  the spectrum is very similar to amorphous iridium  
169 oxide (see Fig. S2c, d). This observation could be understood as a decreased amount of  $\text{Ir}^{\text{VI/V}}$   
170 and the formation of  $\text{Ir}^{\text{III}}$  by intensive leaching and creation of vacancies similar to the  
171 theoretical model mentioned earlier in this section.

172 The O 1s spectra in Fig. 2b confirm that exclusively crystalline  $\text{IrO}_2$  contains  
173 oxygen atoms in the rutile lattice at a binding energy of  $\sim 530$  eV. In perovskites and  
174 amorphous oxide, the binding energy of the main peak is shifted to positive values, which is  
175 usually assigned to hydroxyl groups.<sup>4</sup> Alternatively, it could be attributed to oxygen atoms

176 with different environment, e.g. activated oxygen atoms. The shoulder at 529 eV for  
177  $\text{Ba}_2\text{PrIrO}_6$  results from lattice oxygen bound to the Pr atom<sup>2</sup> and disappears after extensive  
178 leaching (see Fig. S2). Similar absorption features were observed by Reier *et al.*<sup>4</sup> in the case  
179 of  $\text{IrNiO}_x$  and explained by “oxygen hole” states induced by substitution of  $\text{Ir}^{4+}$  with  $\text{Ni}^{2+}$ .<sup>36</sup>

180 We suggest that the presence of activated oxygen atoms is crucial for the  
181 explanation of the following results in activity and dissolution. The dense packing of the rutile  
182 structure restricts the formation of activated oxygen atoms to the surface, which is  
183 undercoordinated by definition. In contrast, for porous hydrous oxides with intercalated water  
184 molecules<sup>37,38</sup> iridium atoms inside the structure can participate in the reaction. These centres  
185 are surrounded by a higher number of activated oxygen atoms and weaker in coordination  
186 facilitating their instability (see discussion on mechanism and Stability-number).

187



188  
189 **Figure 2. XPS results of pristine  $\text{Ba}_2\text{PrIrO}_6$ , amorphous  $\text{IrO}_x$  and crystalline  $\text{IrO}_2$ .** (a) Ir 4f and (b) O 1s  
190 spectra. Additional results of the leached  $\text{Ba}_2\text{PrIrO}_6$  are presented in the supporting information (Fig. S2).

191

192

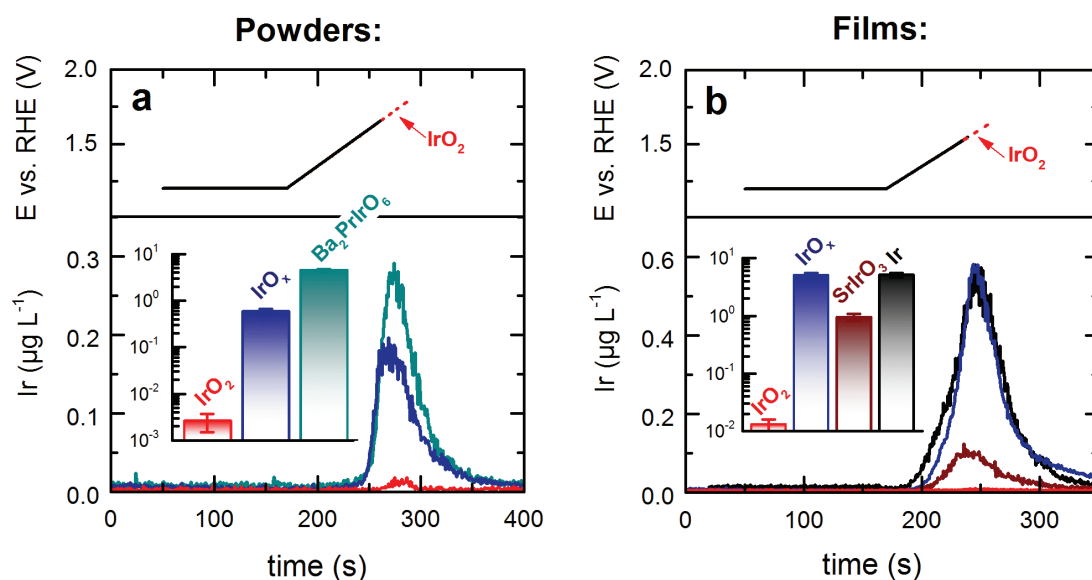
193

194

195

## 196 Stability and activity with respect to OER

197 The SFC coupled to ICP-MS analytics enables in situ detection of dissolved iridium  
198 ions during the oxygen evolution. This approach was used to investigate film and powder  
199 materials by performing a linear sweep of potential at  $5 \text{ mV s}^{-1}$ , illustrated in Fig. 3a and 3b.  
200 Potential and dissolution are plotted on the same time scale. The insets present the integrated  
201 amount on a logarithmic scale. In line with previous reports we recorded orders of magnitude  
202 higher dissolution for metallic iridium and hydrous iridium oxide in comparison to crystalline  
203 iridium oxide.<sup>10,39</sup> Perovskites, additionally studied in this work, show as well high  
204 dissolution in the range of amorphous/hydrous oxide and therefore might not be suitable for  
205 long time operation. Still, the high activity of the latter, demonstrated in the following, is of  
206 importance to understand the clues on the synthesis of an improved OER catalyst.  
207



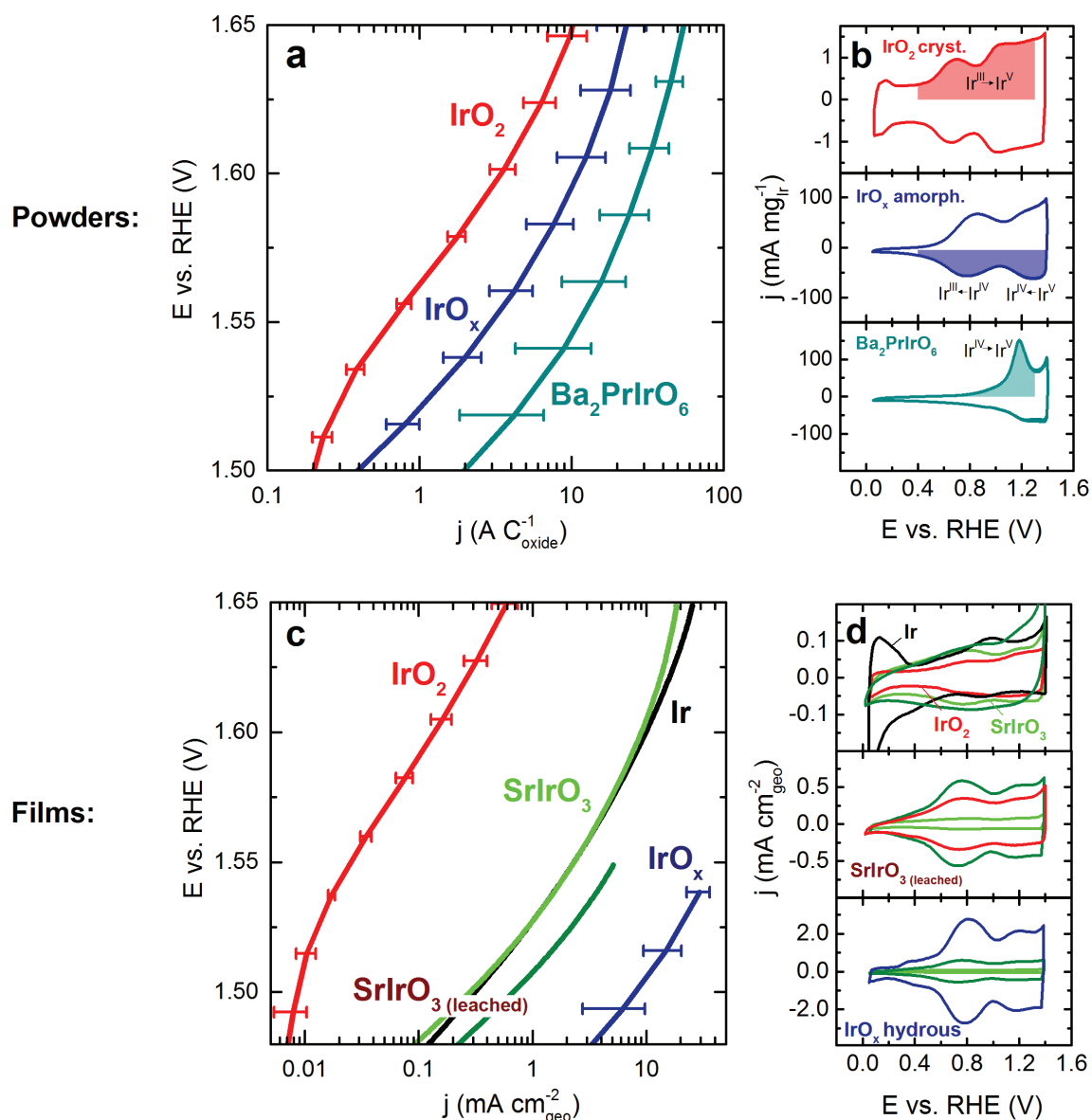
208  
209 **Figure 3. Investigation of iridium dissolution during OER.** (a) Detected iridium concentration in the  
210 electrolyte during the 2<sup>nd</sup> linear scan of potential to 1.65 V vs. RHE for investigated powders. In case of IrO<sub>2</sub> a  
211 higher loading was used and the potential was increased to 1.8 V vs. RHE in order to reach iridium  
212 concentrations above the detection limit of the ICP-MS. Inset: integrated dissolution normalized by the actual  
213 mass of iridium loaded given in  $\text{ng } \mu\text{g}_{\text{Ir}}^{-1}$ . (b) Detected iridium concentration in the electrolyte during a linear  
214 scan of potential to 1.55 V vs. RHE for investigated films. In case of IrO<sub>2</sub> the potential was increased to 1.65 V  
215 vs. RHE. Inset: integrated dissolution normalized to the geometric surface area given in  $\text{ng cm}^{-2}$ .

216  
217  
218  
219

220 In order to take into account the different active surface areas of the samples the  
221 OER-current is normalized to the pseudocapacitive charge  $Q_{\text{oxide}}$  extracted from the cyclic  
222 voltammograms in the range of 0.4 to 1.3 V vs. RHE (Fig. 4).  $Q_{\text{oxide}}$  is considered as a fair  
223 approximation<sup>40-43</sup> for the number of involved active sites, avoiding misinterpretation of data  
224 on activity due to surface area effects. Based on the position of the redox peak in Fig. 4b we  
225 assume that predominantly  $\text{Ir}^{\text{IV}}/\text{Ir}^{\text{V}}$  transition<sup>37,44</sup> appears in perovskites while  $\text{Ir}^{\text{III}}/\text{Ir}^{\text{IV}}$  is  
226 suppressed. In commercial amorphous  $\text{IrO}_x$  the  $\text{Ir}^{\text{III}}/\text{Ir}^{\text{IV}}$  redox peak is much more pronounced  
227 with a second wave indicating further oxidation to  $\text{Ir}^{\text{V}}$ . Assuming that  $\text{Ir}^{\text{V}}$  is essential for fast  
228 OER kinetics, high presence of this species in perovskites could explain their superior activity  
229 in comparison to  $\text{IrO}_x$  and  $\text{IrO}_2$ . Alternatively the numerous activated oxygen atoms present in  
230  $\text{Ba}_2\text{PrIrO}_6$  due to complete isolation of  $\text{IrO}_6$  octahedral after leaching could be the reason for a  
231 boost in specific activity. Normalization of OER activity to the actual mass of iridium is  
232 shown in Fig. S5. Even though perovskite particles tested in this work are large in size (Fig.  
233 S4), high activities were achieved, which is another indication on the formation of a very  
234 active and highly porous layer.

235 In Fig. 4c and 4d the analogous procedure is illustrated for sputtered samples. Low  
236 roughness of these films allows normalization to geometric surface area. Exceptions are  
237 leached  $\text{SrIrO}_3$  and electrochemically grown hydrous iridium oxide, investigated numerously  
238 in the literature.<sup>31,45,46</sup> Both show enhanced pseudo capacitance assigned to the formation of a  
239 porous hydrous oxide layer. Almost identical CV shapes are indications on very similar  
240 structures of the latter. The extraordinary activity of these porous 3D-structures is, inter alia,  
241 related to the high number of accessible active sites. Normalization to pseudocapacitive  
242 charge, as mentioned for powder samples, is necessary to reveal further insights on the  
243 specific activity. The trend for specific activity is:  $\text{Ba}_2\text{PrIrO}_6 > \text{SrIrO}_3 = \text{IrO}_x > \text{IrO}_2$ ,  
244 presented and discussed in the supporting information (Figs. S6 –S8). Focusing on the flat  
245 samples of iridium metal, crystalline  $\text{IrO}_2$  and pristine  $\text{SrIrO}_3$  with similar  $Q_{\text{oxide}}$  (Fig. 4d) one  
246 can conclude that the specific OER activity on  $\text{SrIrO}_3$  and metallic iridium is about two orders  
247 of magnitude higher in comparison to crystalline  $\text{IrO}_2$ , caused by a thin hydrated oxide layer  
248 formed on  $\text{SrIrO}_3$  via leaching and metallic iridium via surface oxidation during OER,<sup>45</sup>  
249 which is not present for crystalline iridium oxide.

250



251  
 252 **Figure 4. Comparison of the investigated materials in terms of activity.** (a) OER-activity of the powder  
 253 materials recorded with a linear scan of potential at  $5 \text{ mV s}^{-1}$  (iR-drop corrected). The current is normalized to  
 254 the pseudocapacitive charge in the anodic scan between 0.4 and 1.3  $\text{V}_{\text{RHE}}$  at  $200 \text{ mV s}^{-1}$ . (b) Cyclic  
 255 voltammograms recorded with  $200 \text{ mV s}^{-1}$ , the integrated area of the oxide charge used for normalization is  
 256 highlighted. (c) OER-activity of the investigated films recorded with a linear scan of potential at  $5 \text{ mV s}^{-1}$ . The  
 257 current is normalized to the geometric surface area. (d) Cyclic voltammograms recorded with  $200 \text{ mV s}^{-1}$ . All  
 258 measurements were carried out in  $0.1 \text{ M HClO}_4$  purged with argon.

259  
 260  
 261  
 262  
 263  
 264

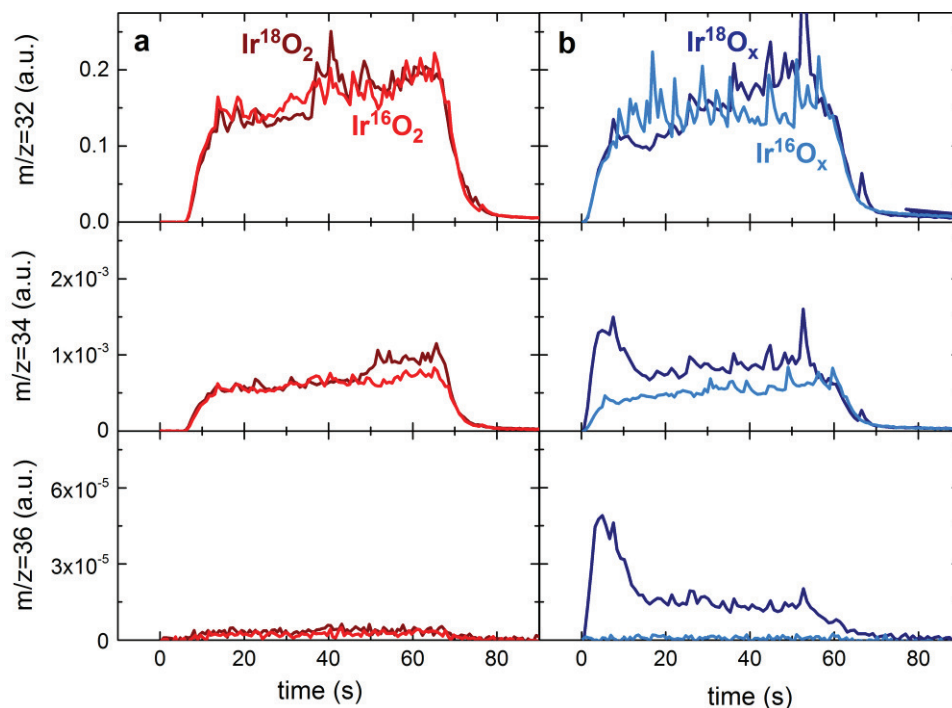
## 265 **Mechanistic insights**

266 With the gained understanding on structure, dissolution, and activity, we want to  
267 combine existing mechanisms of the OER on iridium-based catalysts<sup>47-51</sup> with a mechanism  
268 for simultaneous dissolution. Starting point is the differentiation of two oxygen species  
269 present either in crystalline iridium oxide or amorphous, hydrated iridium oxides and the  
270 significantly higher stability of the crystalline structure in comparison to the amorphous  
271 hydrated structure as presented in Fig. 3.

272 The case of amorphous hydrous oxide merits special attention, as its structure is still  
273 unknown. According to Pfeifer *et al.*,<sup>51-53</sup> enhanced activity of amorphous iridium oxide is  
274 caused by electrophilic O<sup>-</sup> species that are preferred for nucleophilic attack by water,  
275 reducing the activation energy for the adsorption. Grimaud *et al.*<sup>29</sup> came to similar  
276 conclusions using La<sub>2</sub>LiIrO<sub>6</sub> as a model catalyst. There are several indications that the  
277 “activated oxygen atoms” as described in this work and the abovementioned “O<sup>-</sup> species” are  
278 indeed interchangeable. The presence of O<sup>-</sup> is, however, counterintuitive, as the high  
279 electronegativity of oxygen in comparison to iridium should hardly allow the allocation of a  
280 formal oxidation state of -1. Based on structural investigation of different amorphous iridium  
281 oxides (e.g. hollandites), Willinger *et al.*<sup>54</sup> concluded that the ratio between corner- and edge-  
282 sharing IrO<sub>6</sub> octahedra is determining the OER activity. Thus, a high number of corner  
283 sharing oxygen atoms (activated oxygen) facilitates the OER. Regardless of the formal  
284 oxidation state and termination, it was experimentally proven by <sup>18</sup>O labelling for Co-based  
285 perovskites, that activated oxygen can participate in the OER, which was taken as evidence  
286 for oxygen redox chemistry.<sup>50</sup> Furthermore it is an important argument to explain the  
287 instability of amorphous iridium oxides. In the following, the term lattice oxygen accounts  
288 generally for all oxygen atoms that are part of the structure and is not exclusively limited to  
289 the described oxygen atoms of the rutile lattice. Evidence for the participation of oxygen from  
290 the lattice of iridium oxides is rare. One work of Fierro *et al.*<sup>55</sup> contains indications on a  
291 participation, however, it focuses only on one type of oxide, the exact nature of which  
292 remains unclear and therefore does not allow further generalization and conclusions.

293 In order to resolve the extent of lattice oxygen participation during OER on rutile and  
294 amorphous iridium oxides (the final state for all unstable iridium-based oxides) in more detail  
295 a method of isotope labelling combined with online electrochemical mass spectrometry was  
296 used. The labelled Ir<sup>18</sup>O<sub>2</sub> and Ir<sup>18</sup>O<sub>x</sub> films (for preparation see methods section) were  
297 polarized galvanostatically in H<sub>2</sub><sup>16</sup>O-based electrolyte and formation of volatile species with

298 mass to charge ratios of 32 ( $^{16}\text{O}^{16}\text{O}$ ), 34 ( $^{16}\text{O}^{18}\text{O}$ , and to a small extent  $^{17}\text{O}^{17}\text{O}$ ) and 36  
 299 ( $^{18}\text{O}^{18}\text{O}$ ) were measured online (see Fig. 5). In order to compensate the influence of naturally  
 300 occurring  $\text{H}_2^{18}\text{O}$  isotopes in the  $\text{H}_2^{16}\text{O}$ -based electrolyte, the same protocol was applied to  
 301 unlabelled rutile  $\text{Ir}^{16}\text{O}_2$  and hydrous  $\text{Ir}^{16}\text{O}_x$  prepared by identical procedures. During anodic  
 302 polarization, both labelled and unlabelled rutile samples show similar formation of various  
 303 oxygen products (Fig. 5a). This indicates that participation of lattice oxygen in the OER is  
 304 absent or negligible. In contrast, the formation of  $m/z=34$  and  $m/z=36$  on  $\text{Ir}^{18}\text{O}_x$  is more  
 305 intense in comparison to the unlabelled sample (Fig. 5b), denoting the instability of  
 306 amorphous oxide lattice towards OER. However, the low measured intensities of  $m/z=34$  and  
 307  $m/z=36$  suggest that the major part of the evolved oxygen molecules is formed via water  
 308 discharge. Gradual decrease of  $m/z=34$  and  $m/z=36$  signals on labelled  $\text{Ir}^{18}\text{O}_x$  indicates an  
 309 exchange between lattice oxygen atoms and oxygen from water induced by the OER.  
 310



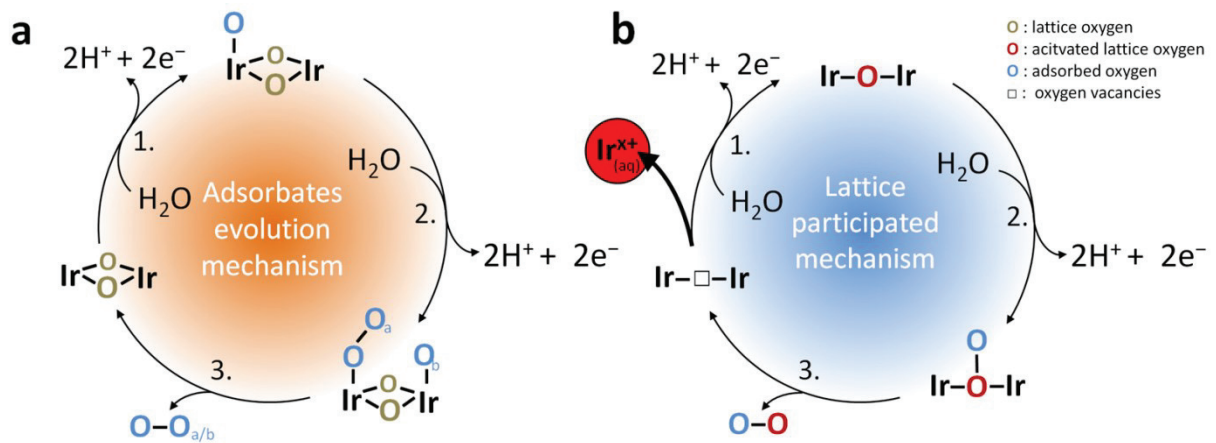
311  
 312 **Figure 5. Online observation of lattice oxygen evolution on (a) rutile  $\text{Ir}^{18}\text{O}_2$  /  $\text{Ir}^{16}\text{O}_2$  and (b) hydrous  $\text{Ir}^{18}\text{O}_x$  /**  
 313  **$\text{Ir}^{16}\text{O}_x$  films during 60 s of anodic polarization at  $25 \text{ mA cm}^{-2}_{\text{geo}}$ . The signals from  $m/z$  of 32, 34 and 36**  
 314 **correspond to  $^{32}\text{O}_2$ ,  $^{34}\text{O}_2$  and  $^{36}\text{O}_2$ , respectively. Electrolyte: 0.1 M  $\text{HClO}_4$  in  $\text{H}_2^{16}\text{O}$ .**  
 315

316 Based on the results shown in Fig. 5 and additional data presented in literature, we  
 317 propose a summarized view on the OER mechanisms in Fig. 6. On the left side, the classical  
 318 mechanism on crystalline iridium oxide is presented as adsorbates evolution mechanism.<sup>47-49</sup>  
 319 The reaction can either happen on a single iridium site via an OOH intermediate<sup>34,56</sup> (acid-

320 base)<sup>48,57</sup> or by the coupling of two oxygen atoms from different sites (direct coupling).<sup>58</sup> For  
321 the cycle on the right side, we base ourselves on the mechanism proposed by Grimaud *et al.*<sup>50</sup>  
322 and Rong *et al.*<sup>49</sup> Here, the reaction pathway differs by participation of activated (lattice)  
323 oxygen in the reaction. It is assumed to be operative in the case of amorphous IrO<sub>x</sub> and in  
324 leached perovskites. The activated oxygen is attacked by water (step 2) and removed as O<sub>2</sub>  
325 from the surface (step 3) leaving behind an oxygen vacancy.<sup>49,50,59</sup> This can either happen  
326 with one lattice oxygen or by combining two lattice oxygen atoms as shown in Fig. 5b,  
327 resulting in an iridium atom with two vacancies, which is highly probable to dissolve. The  
328 latter scenario is less likely to happen for crystalline oxide. Participation of lattice oxygen, if  
329 at all, is restricted to the outer surface while bulk oxygen will not participate and maintain a  
330 high coordination of the iridium atom, resulting in a significantly lower probability for the  
331 iridium atom to dissolve out of the structure. To close the cycle vacancies can be refilled by  
332 adsorption of water or bulk oxygen migration<sup>29</sup> (step 1). We suggest the lower activation  
333 energy for the adsorption of water in vacancies is further contributing to the higher activity of  
334 amorphous oxide structures. Simultaneously, the weak bonding of iridium next to an oxygen  
335 vacancy is considered as the reason for dissolution of iridium in amorphous iridium oxide  
336 structures. In case more vacancies are created at the same time on one iridium atom,  
337 dissolution becomes even more preferable. Dissolution itself might take place without  
338 electron transfer Ir<sup>III</sup><sub>(oxide)</sub> → Ir<sup>3+</sup><sub>(aq)</sub>. A similar reaction pathway was proposed recently by our  
339 group, in which the existence of an Ir<sup>III</sup> intermediate in the OER cycle was linked to the  
340 dissolution of hydrous iridium oxide.<sup>60</sup> Alternatively, additional electron transfer would lead  
341 to formation of IrO<sub>3</sub> and IrO<sub>4</sub><sup>2-</sup>, described elsewhere.<sup>61,62</sup>

342 As crystalline iridium oxide is assigned to the adsorbates evolution mechanism, its  
343 very low but still measurable dissolution is not considered, yet. The constancy of the S-  
344 number presented in the following section (Fig. 7c), suggests a direct relation between the  
345 OER mechanism and the dissolution mechanism. The origin of the crystalline iridium oxide  
346 dissolution might be some limited lattice oxygen participation on the surface similar to the  
347 mechanism in Fig. 5b or other intermediates and dissolution pathways, e.g. formation of  
348 volatile IrO<sub>3</sub>.<sup>61,62</sup> (see further discussion in the SI).

349 In conclusion, a catalyst's stability is determined by (i) the ratio between the two  
350 presented mechanisms (a less stable material has a higher rate in the lattice participated  
351 mechanism) and (ii) the stability of the intermediate itself, which can be higher for a rutile  
352 structure in comparison to the amorphous oxide due to a more compact structure.



354

355

356 **Figure 6. Sketch of the simplified OER reaction mechanism with dissolution pathway.** (a) Classical  
 357 mechanism for crystalline IrO<sub>2</sub> without participation of lattice oxygen. Two possible pathways are presented:  
 358 single site and double site. (b) Mechanism suggested for amorphous iridium oxide and leached perovskites with  
 359 participation of activated oxygen in the reaction forming oxygen vacancies. Weakening the binding of iridium in  
 360 the structure is taken as main reason for enhanced dissolution. To complete the cycle, vacancies can be filled  
 361 again by adsorption of water. Octahedral configuration of iridium is not presented completely as well as  
 362 nucleophilic attack of water and removal of proton is merged to one step to not overcrowd the scheme.

363

364

### 365 **The Stability-number**

366 Significantly higher dissolution rates of iridium, but also higher OER rates were  
 367 observed for amorphous IrO<sub>x</sub> and perovskites in comparison to crystalline IrO<sub>2</sub>. In order to  
 368 take into account the possible effect of much higher amount of oxygen formed on amorphous  
 369 and perovskite structures on dissolution, we introduce a metric characterizing the activity vs.  
 370 stability performance of a given catalyst. The so called Stability-number (S-number) is  
 371 defined as the ratio between the amount of evolved oxygen (calculated from  $Q_{\text{total}}$ ) and the  
 372 amount of dissolved iridium (extracted from ICP-MS data). The S-number describes how  
 373 many oxygen molecules are formed per one iridium atom lost into the electrolyte.  
 374 Consequently it is independent of the amount of involved active sites, surface area, or catalyst  
 375 loading and gives an illustrative comparison of the stability of various materials. Moreover,  
 376 unlike current efficiency, the S-number can be calculated without knowing the exact nature of  
 377 the dissolved species and can be applied to neutral species. The higher the number, the more  
 378 stable is the active centre of the electrocatalyst. Based on dissolution measurements presented  
 379 in Fig. 3, the highest S-numbers were calculated for crystalline IrO<sub>2</sub> (Fig. S9). Perovskite

380 based iridium oxides possess the lowest S-numbers with two orders of magnitude less oxygen  
381 evolved per dissolved iridium compared to rutile IrO<sub>2</sub>. However, the influence of initially  
382 dissolved iridium from defects as well as possible stabilization during longer operation should  
383 not be overlooked in these short measurements (see discussion Fig. S10).

384 In order to demonstrate a more relevant study on stability of the investigated powders  
385 and to gain further understanding on possible correlations of OER-mechanism and dissolution  
386 mechanism, we varied the current per mass of iridium using galvanostatic steps of ~5-20 min  
387 until a steady dissolution rate was observed (see Fig. S11). According to Fig. 7a the S-  
388 numbers match the ones presented in the supporting information using a short linear scan of  
389 potential. Over a wide range of current densities (0.01 to 1 A mg<sub>Ir</sub><sup>-1</sup>) fairly constant S-  
390 numbers were observed, indicating a direct relation between oxygen evolution and dissolution  
391 for all materials. The difference in the absolute value of the S-number can be assigned to: (i) a  
392 weaker bonding of the lattice oxygen in amorphous structures compared to crystalline ones,  
393 enabling a direct participation in the OER with the formation of metastable, activated iridium  
394 complexes that are more prone to dissolution, (ii) the amount of activated oxygen atoms  
395 surrounding one iridium centre, which is assumed to be higher in the case of leached  
396 Ba<sub>2</sub>PrIrO<sub>6</sub> (see Fig. 1e) in comparison to amorphous iridium oxides and rutile IrO<sub>2</sub>, enabling  
397 the occurrence of instable iridium centres with two oxygen vacancies caused by  
398 recombination of two activated oxygen atoms.<sup>50</sup> For crystalline IrO<sub>2</sub> the number of activated  
399 oxygen atoms is restricted to the outer surface while bulk oxygen will not participate and  
400 maintain a high coordination of the iridium atom resulting in a significantly lower probability  
401 for the iridium atom to dissolve out of the structure.

402 The constancy of the S-number, observed over a wide range of current densities allows  
403 a relation of dissolution and lifetime of the catalyst using equation 1, presented in Fig. 7b.

$$t = \frac{S \cdot z \cdot F \cdot m}{j \cdot M} \quad (1)$$

404  $t$  = lifetime of the catalyst (s),  $S$  = Stability-number,  $z$  = electrons per transferred O<sub>2</sub>,  
405  $F$  = Faraday constant (96485 C mol<sup>-1</sup>),  $m$  = loaded mass of iridium (g cm<sup>-2</sup>),  $j$  = applied  
406 current density (A cm<sup>-2</sup>),  $M$  = molar mass of iridium (192.2 g mol<sup>-1</sup>).

407

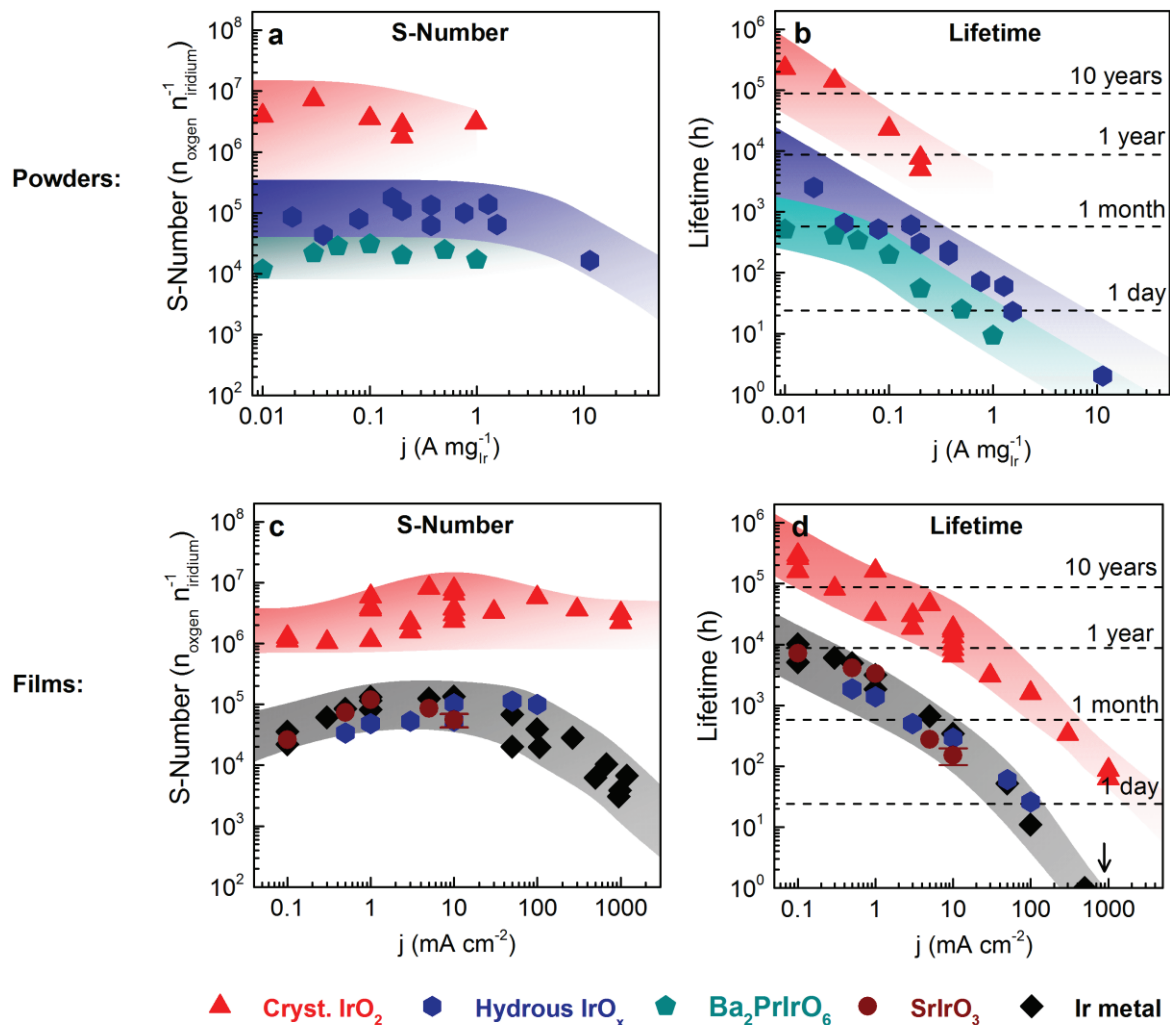
408 Hereby, lifetimes of a few days (Ba<sub>2</sub>PrIrO<sub>6</sub>), one month (IrO<sub>x</sub>) and one year (IrO<sub>2</sub>) were  
409 obtained when considering a constant current density of 0.2 A mg<sub>Ir</sub><sup>-1</sup>. Note these findings are

410 specific for the electrochemical cell used. Lifetimes in a PEM system can deviate, which is  
411 discussed in more detail in the supporting information (see Fig. S12 and related text).

412 In order to widen our scope, also sputtered films were investigated using the same  
413 procedure (Fig. 7c). The trends resemble the ones observed for powders. Additionally, S-  
414 numbers for sputtered metallic iridium are presented, which drop at current densities above 50  
415 mA cm<sup>-2</sup>. A similar trend was observed for IrO<sub>x</sub> in Fig. 7a. The reason is the onset of a second  
416 dissolution pathway forming IrO<sub>4</sub><sup>2-</sup>, which is expected to occur at potentials > 1.8 V vs. RHE<sup>9</sup>  
417 (see Fig. S13). Through kinetic stabilization, the latter pathway is successfully suppressed for  
418 rutile IrO<sub>2</sub> at even higher potentials (reported as well for the hydrogen region<sup>39</sup>). For metallic  
419 iridium and amorphous iridium oxide, a self-accelerating degradation process can be observed  
420 when a critical current density is reached by insufficient loading or degraded catalyst. The  
421 degradation of IrO<sub>2</sub>, however, is exclusively linked to the amount of oxygen evolved and not  
422 to the applied potential.

423

424



425  
 426 **Figure 7.** Investigation of S-Number and lifetime depending on the current load. (a, c) Stability-number (S-  
 427 Number) plotted versus mass specific current density for powders (a) and geometric current density for sputtered  
 428 films (c).  $\text{Ba}_2\text{PrIrO}_6$  was leached for 5 days in advance. (b, d) Calculation of the catalyst's lifetime, based on  
 429 equation 1 for powders (b) and films (d). This approach assumes “steady state” dissolution and neglects  
 430 increased dissolution towards the end of life due to loss of surface area. In case of powder materials  $m$  equals the  
 431 mass of loaded iridium. In case of films  $m$  was set to  $50 \mu\text{g}_{\text{Ir}} \text{cm}^{-2}$  which equals film thicknesses of about 100 nm  
 432  $\text{SrIrO}_3$ , 50 nm  $\text{IrO}_2$ , and 20 nm iridium metal. Measurements were carried out in 0.1 M  $\text{HClO}_4$ .

433  
 434  
 435  
 436  
 437  
 438  
 439

### 440 3. Conclusion

441 In this work, a new metric for stability benchmarking of electrocatalysts, the so called S-  
442 number is introduced, enabling direct evaluation of lifetimes, illustrative comparison of  
443 stability properties, and insights into degradation mechanisms. This concept can be adapted to  
444 a wide range of electrochemical reactions and can be understood as an electrochemical turn  
445 over number (TON) known from the field of heterogeneous catalysis.

446 Moreover, for the first time the in situ dissolution of various iridium-based oxides  
447 including highly crystalline, perovskite-based, and amorphous structures over a wide range of  
448 current densities is presented. The measurements were carried out in acidic electrolyte with  
449 iridium-based perovskites undergoing severe leaching. Hence, in acidic conditions,  
450 explanations for the enhanced activity based on electronic interactions with rare earth or alkali  
451 elements are debatable. The resulting amorphous iridium oxide, which is part of several  
452 studies on innovative OER materials,<sup>1-5</sup> shows exceptional high activity accompanied by high  
453 iridium dissolution. We demonstrate the participation of activated lattice oxygen atoms as  
454 trigger for the boost in activity and the high dissolution rate due to arising oxygen vacancies.

455 Based on our findings, future research in this field should be devoted to formation of  
456 ultrathin films of crystalline iridium oxide on stable and conductive substrates with high  
457 surface area, such as fluorine doped tin oxide (FTO), antimony doped tin oxide (ATO) or  
458 similar materials.<sup>63</sup> By doing so the lower intrinsic activity and the fact that exclusively the  
459 surface of the material is participating in the reaction could be compensated. In case the  
460 superior activity of amorphous iridium oxides is utilized, stabilization of the weak iridium  
461 intermediate caused by oxygen vacancies will be of great importance. Further fundamental  
462 research in understanding dissolution processes of amorphous iridium oxides will be essential  
463 to reach this goal.

464

465

466

467

468

469

## 470 **Methods**

471 **Powder materials.**  $A_2B\text{IrO}_6$  (A= Pr, Nd or Y; B = Ba or Sr) double perovskites were  
472 synthesized in alumina crucibles using  $\text{BaCO}_3$ ,  $\text{SrCO}_3$ ,  $\text{Pr}_6\text{O}_{11}$ ,  $\text{Nd}_2\text{O}_3$ ,  $\text{Y}_2\text{O}_3$  and metallic  
473 iridium powder, respectively. The standard solid-state reactions are described in the  
474 literature.<sup>35</sup> All reactions were carried out in air and the products were furnace-cooled to room  
475 temperature. The powders were intermittently reground during the synthesis. Amorphous  
476 iridium oxide (iridium (IV) oxide dihydrate) and crystalline iridium oxide (iridium (IV)  
477 oxide) were purchased from Alfa Aesar. To ensure complete crystallisation, iridium (IV)  
478 oxide was additionally calcined at 600°C for 48 h in air.

479 For powder samples the electrodes were prepared by dropcasting 0.3  $\mu\text{L}$  suspension on a  
480 glassy carbon plate. All suspensions contained the same amount of iridium (0.27  $\text{mg mL}^{-1}$ ).  
481 For some measurements of crystalline  $\text{IrO}_2$ , however, the concentration was enhanced to 4.5  
482  $\text{mg mL}^{-1}$  in order to exceed the detection limit of the ICP-MS and measure reasonable  
483 currents in the cyclic voltammograms. To avoid detachment 20  $\mu\text{L}$  of Nafion solution (5 w%,  
484 Sigma-Aldrich) was added to 5 mL of suspension. The dried spots ( $\varnothing \sim 1$  mm) were rinsed  
485 with water and located with the help of a vertical camera attached to the SFC. The  
486 measurements were carried out by placing the spot in the centre of the SFC's opening area  
487 ( $A = 0.035 \text{ cm}^2$ ).

488  
489 **Film materials.** Ir metal films were deposited by physical vapour deposition in a magnetron  
490 sputter system (AJA ATC 2200-V) with a confocal target setup. The 100 nm thick Ir film was  
491 deposited on a thermally oxidized (1.5  $\mu\text{m SiO}_2$ ) 4-inch diameter Si (100) wafer with an  
492 intermediate, 10 nm thick, Ti adhesion layer. Sputter targets were pre-cleaned at 150 W direct  
493 current (DC), 4 Pa, 300 s for Ti and 100 W DC, 4 Pa, 30 s for Ir. The deposition was  
494 performed at 150 W DC, 1.3 Pa, 150 s for Ti and 60 W DC, 0.66 Pa, 1200 s for Ir. Both layers  
495 were deposited with substrate rotation. The sputter system was operated with a base pressure  
496  $<2.6 \times 10^{-5}$  Pa and an Ar plasma.

497 For high current density measurements on iridium metal, lift-off photolithography was used to  
498 structure the thin film and create small catalyst dots (see Fig. S14). By doing so the bubble  
499 detachment in the SFC was facilitated significantly. For the lift-off a bilayer photoresist  
500 system consisting of an LOR 20 B (MicroChem) bottom and an AZ 1518 (MicroChemicals)  
501 top layer was utilized. After deposition the photoresist was removed in a cleaning cascade of  
502 acetone and isopropanol under ultrasonic agitation.

503 Hydrous IrO<sub>x</sub> films were grown on the sputtered iridium spots by 300 square wave pulses of  
504 0.5 s between 0.05 V and 1.4 V vs. RHE.

505 Crystalline IrO<sub>2</sub> films were produced on Si/SiO<sub>2</sub> wafers via reactive sputtering in the presence  
506 of O<sub>2</sub> using a DC magnetron sputtering machine (BesTech GmbH, Berlin) followed by  
507 additional thermal treatment at 600°C for 48 h in air.

508 SrIrO<sub>3</sub> film samples were epitaxially grown using on-axis, RF magnetron sputtering of a  
509 Sr<sub>4</sub>IrO<sub>6</sub> target on (001) SrTiO<sub>3</sub>. Due to two-dimensional growth, the surface of the samples  
510 was atomically flat, with 0.4 nm steps corresponding to the pseudo-cubic cell parameter. X-  
511 ray diffraction showed that the films were single crystals, oriented [110] perpendicular to the  
512 substrate<sup>64</sup>.

513 **Labelled samples.** Thin films of isotope labelled reactively sputtered Ir<sup>18</sup>O<sub>2</sub> were deposited  
514 by magnetron sputtering (BesTech GmbH, Berlin) at 100 W in a mixture of <sup>18</sup>O<sub>2</sub> (99.00 at.%,  
515 Sigma Aldrich) and Ar as the sputter gas and the chamber pressure was regulated to 0.5 Pa at  
516 room temperature. The base vacuum before deposition was 2.0x10<sup>-6</sup> Pa. The Ø3 inch target of  
517 Ir (99.9%, Evochem) was pre-cleaned by sputtering against closed shutters prior to  
518 deposition. To prepare films with a minimal surface roughness, on the smooth substrates of  
519 single crystalline Si(100) wafers with a 1.5 µm thermal SiO<sub>2</sub> diffusion and reaction barrier  
520 layer were used. The resulting thickness of the obtained coating was approximately 80 nm.  
521 After the deposition films were annealed in vacuum at 500°C during 2 hours. Unlabelled  
522 reactively sputtered Ir<sup>16</sup>O<sub>2</sub> were deposited using a mixture of <sup>16</sup>O<sub>2</sub> and Ar. All other  
523 conditions were kept as described before.

524 The <sup>18</sup>O-labelled samples of hydrous Ir<sup>18</sup>O<sub>x</sub> were prepared using a solution of 0.1 M HClO<sub>4</sub> in  
525 H<sub>2</sub><sup>18</sup>O (97.76 at.%, Campro Scientific GmbH) applying a square wave potential program with  
526 upper and lower potential limits of 1.4 and 0.04 V vs. RHE, respectively (600 cycles at 0.5  
527 Hz) to a sputtered Ir film (see description above). Afterwards the electrodes were carefully  
528 rinsed with ultrapure H<sub>2</sub><sup>16</sup>O water and threated in the vacuum at 80°C during 2 hours.  
529 Unlabelled samples were prepared using electrolyte containing 0.1 M HClO<sub>4</sub> (Suprapur<sup>®</sup> 70%  
530 HClO<sub>4</sub>, Merck) in ultrapure H<sub>2</sub><sup>16</sup>O water (PureLab Plus system, Elga, 18 MΩcm, TOC < 3  
531 ppb), using the same electrochemical program.

532 All <sup>18</sup>O-labelled samples were prepared right before the OLEMS measurements and  
533 transferred in a desiccator to avoid exchange of lattice oxygen in topmost layers with air.

534

535 **Electrochemical measurements.** Dissolution measurements were performed in argon purged  
536 0.1 M HClO<sub>4</sub> using a scanning flow cell (SFC) connected to an inductively coupled plasma  
537 mass spectrometer (ICP-MS)<sup>65</sup>. A graphite rod and an Ag/AgCl electrode (Metrohm,  
538 Germany) were used as counter and reference electrode, respectively. The electrolyte was  
539 prepared by dilution of concentrated acid (Suprapur<sup>®</sup> 70% HClO<sub>4</sub>, Merck) in ultrapure water  
540 (PureLab Plus system, Elga, 18 MΩ cm, TOC < 3 ppb). Flow rate through the cell was 352  
541 μL min<sup>-1</sup>. Steady performance of the ICP-MS (NexION 300X, Perkin Elmer) was ensured by  
542 addition of internal standard solution (<sup>187</sup>Re, <sup>130</sup>In) downstream to the flow cell and daily  
543 calibration. A scheme of the SFC is presented in the supporting information (Fig. S14).  
544 OLEMS (online electrochemical mass spectrometer) measurements were carried out using a  
545 SFC – set up, previously described elsewhere.<sup>66</sup> In contrast to the SFC connected to ICP-MS,  
546 here the surface area of the working electrode was 0.125 cm<sup>2</sup> and a PTFE tip from the top of  
547 the cell through an extra vertical channel was introduced. A 50 μm thick PTFE Gore-Tex  
548 membrane with a pore size of 20 nm, through which products can evaporate into the vacuum  
549 system of the mass spectrometer (Max 300 LG, Extrel) was mounted onto the very end of the  
550 tip. The approximate distance from the tip to the electrode was about 50 μm, which is  
551 determined by the thickness of the silicon ring sealing around the cell opening and the applied  
552 contact force. These parameters were kept constant during the whole set of measurements.  
553 A potentiostat (Reference 600, Gamry) was used for the electrochemical measurements with  
554 both setups.

555  
556 **Materials characterisation.** Scanning electron microscopy (SEM) measurements were  
557 performed in secondary electron mode using a Leo 1550 VP (Zeiss) operated at 15 kV and 6  
558 mm sample distance. For energy-dispersive X-ray spectroscopy (EDS) the acceleration  
559 voltage was increased to 30 kV.

560 Measurements of x-ray photoelectron spectra were performed applying a monochromatic Al  
561 Kα X-ray source (1486.6 eV) operating at 15 kV and 25 W (Quantero II, Physical Electronics,  
562 Chanhassen, MN, USA). The binding energy scale was referenced to the C 1s signal at 285.0  
563 eV.

564 TEM and SAED analysis were performed with a CM20 FEG electron microscope (from  
565 Philips) operated at 200 kV. The samples were prepared by dropcasting about 5 μl of catalyst  
566 suspension onto a gold TEM grid coated with a Lacey carbon film (NH7, Plano GmbH).

567

## 568 **Data availability**

569 The authors declare that the main data supporting the findings of this study are available  
570 within the article and its Supplementary Information file. Extra data are available from the  
571 corresponding authors upon request.

572

## 573 **Acknowledgements**

574 The authors acknowledge funding by the German Federal Ministry of Education and Research  
575 (BMBF) within the Kopernikus Project P2X and a further project (Kz: 033RC1101A). S. G.  
576 acknowledges financial support from BASF. O.K. acknowledges financial support from the  
577 Alexander von Humboldt Foundation. K. M. acknowledges financial support from the DFG  
578 under the project number MA4819/4-1. L. F. and Z. L. acknowledge support from the Agence  
579 Nationale de la Recherche grant SOCRATE ANR-15-CE30-0009-01. Additional thanks go to  
580 Katharina Hengge and Thomas Gänsler for carrying out the TEM and SAED measurements.

581

## 582 **References**

- 583 1 Seitz, L. C. *et al.* A highly active and stable IrO<sub>x</sub>/SrIrO<sub>3</sub> catalyst for the oxygen  
584 evolution reaction. *Science* **353**, 1011-1014, doi:10.1126/science.aaf5050 (2016).
- 585 2 Diaz-Morales, O. *et al.* Iridium-based double perovskites for efficient water oxidation  
586 in acid media. *Nature communications* **7**, 12363, doi:10.1038/ncomms12363 (2016).
- 587 3 Nong, H. N. *et al.* Oxide-supported IrNiO(x) core-shell particles as efficient, cost-  
588 effective, and stable catalysts for electrochemical water splitting. *Angewandte Chemie*  
589 **54**, 2975-2979, doi:10.1002/anie.201411072 (2015).
- 590 4 Reier, T. *et al.* Molecular Insight in Structure and Activity of Highly Efficient, Low-Ir  
591 Ir-Ni Oxide Catalysts for Electrochemical Water Splitting (OER). *J Am Chem Soc*  
592 **137**, 13031-13040, doi:10.1021/jacs.5b07788 (2015).
- 593 5 Lettenmeier, P. *et al.* Nanosized IrO(x)-Ir Catalyst with Relevant Activity for Anodes  
594 of Proton Exchange Membrane Electrolysis Produced by a Cost-Effective Procedure.  
595 *Angewandte Chemie* **55**, 742-746, doi:10.1002/anie.201507626 (2016).
- 596 6 Sun, W., Song, Y., Gong, X.-Q., Cao, L.-m. & Yang, J. An efficiently tuned d-orbital  
597 occupation of IrO<sub>2</sub> by doping with Cu for enhancing the oxygen evolution reaction  
598 activity. *Chem. Sci.* **6**, 4993-4999, doi:10.1039/c5sc01251a (2015).
- 599 7 Sun, W. *et al.* OER activity manipulated by IrO<sub>6</sub> coordination geometry: an insight  
600 from pyrochlore iridates. *Scientific reports* **6**, 38429, doi:10.1038/srep38429 (2016).
- 601 8 Sun, W., Song, Y., Gong, X. Q., Cao, L. M. & Yang, J. Hollandite Structure K(x  
602 approximately 0.25)IrO<sub>2</sub> Catalyst with Highly Efficient Oxygen Evolution Reaction.  
603 *ACS Appl Mater Interfaces* **8**, 820-826, doi:10.1021/acsami.5b10159 (2016).

- 604 9 Pourbaix, M. *Atlas of electrochemical equilibria in aqueous solutions*. (National  
605 Association of Corrosion Engineers, 1974).
- 606 10 Geiger, S. *et al.* Activity and Stability of Electrochemically and Thermally Treated  
607 Iridium for the Oxygen Evolution Reaction. *J. Electrochem. Soc.* **163**, F3132-F3138  
608 (2016).
- 609 11 Cherevko, S. *et al.* Stability of nanostructured iridium oxide electrocatalysts during  
610 oxygen evolution reaction in acidic environment. *Electrochemistry Communications*  
611 **48**, 81-85, doi:10.1016/j.elecom.2014.08.027 (2014).
- 612 12 Abbott, D. F. *et al.* Iridium Oxide for the Oxygen Evolution Reaction: Correlation  
613 between Particle Size, Morphology, and the Surface Hydroxo Layer from Operando  
614 XAS. *Chemistry of Materials* **28**, 6591-6604, doi:10.1021/acs.chemmater.6b02625  
615 (2016).
- 616 13 Beni, G., Schiavone, L. M., Shay, J. L., Dautremont-Smith, W. C. & Schneider, B. S.  
617 Electrocatalytic oxygen evolution on reactively sputtered electrochromic iridium oxide  
618 films. *Nature (London)* **282**, 281-283, doi:10.1038/282281a0 (1979).
- 619 14 Bockris, J. O. M. & Otagawa, T. The Electrocatalysis of Oxygen Evolution on  
620 Perovskites. *J. Electrochem. Soc.* **131**, 290-302 (1984).
- 621 15 Bockris, J. O. M., Otagawa, T. & Young, V. Solid state surface studies of the  
622 electrocatalysis of oxygen evolution on perovskites. *J. Electroanal. Chem.* **150**, 633-  
623 643 (1983).
- 624 16 Kortenaar, M. V., Vente, J. F., Ijdo, D. J. W., Müller, S. & Kötzt, R. Oxygen evolution  
625 and reduction on iridium oxide compounds *Journal of Power Sources* **56**, 51-60  
626 (1995).
- 627 17 Bursell, M., Pirjamali, M. & Kiros, Y. La<sub>0.6</sub>Ca<sub>0.4</sub>CoO<sub>3</sub>, La<sub>0.1</sub>Ca<sub>0.9</sub>MnO<sub>3</sub> and  
628 LaNiO<sub>3</sub> as bifunctional oxygen electrodes. *Electrochim. Acta* **47**, 1651-1660 (2002).
- 629 18 Suntivich, J., May, K. J., Gasteiger, H. A., Goodenough, J. B. & Shao-Horn, Y. A  
630 perovskite oxide optimized for oxygen evolution catalysis from molecular orbital  
631 principles. *Science* **334**, 1383-1385, doi:10.1126/science.1212858 (2011).
- 632 19 Grimaud, A. *et al.* Double perovskites as a family of highly active catalysts for oxygen  
633 evolution in alkaline solution. *Nature communications* **4**, 2439,  
634 doi:10.1038/ncomms3439 (2013).
- 635 20 Rincon, R. A. *et al.* Evaluation of perovskites as electrocatalysts for the oxygen  
636 evolution reaction. *Chemphyschem : a European journal of chemical physics and*  
637 *physical chemistry* **15**, 2810-2816, doi:10.1002/cphc.201402137 (2014).
- 638 21 Petrie, J. R., Jeen, H., Barron, S. C., Meyer, T. L. & Lee, H. N. Enhancing Perovskite  
639 Electrocatalysis through Strain Tuning of the Oxygen Deficiency. *J Am Chem Soc*  
640 **138**, 7252-7255, doi:10.1021/jacs.6b03520 (2016).
- 641 22 Zhu, L., Ran, R., Tade, M., Wang, W. & Shao, Z. Perovskite materials in energy  
642 storage and conversion. *Asia-Pacific Journal of Chemical Engineering* **11**, 338-369,  
643 doi:10.1002/apj.2000 (2016).
- 644 23 Zhu, Y. *et al.* Enhancing Electrocatalytic Activity of Perovskite Oxides by Tuning  
645 Cation Deficiency for Oxygen Reduction and Evolution Reactions. *Chemistry of*  
646 *Materials* **28**, 1691-1697, doi:10.1021/acs.chemmater.5b04457 (2016).
- 647 24 Wu, Z. *et al.* Effect of Sr doping on the electrochemical properties of bi-functional  
648 oxygen electrode PrBa<sub>1-x</sub>Sr<sub>x</sub>Co<sub>2</sub>O<sub>5+δ</sub>. *Journal of Power Sources* **334**, 86-93,  
649 doi:10.1016/j.jpowsour.2016.10.013 (2016).
- 650 25 Chen, D., Wang, J., Zhang, Z., Shao, Z. & Ciucci, F. Boosting oxygen  
651 reduction/evolution reaction activities with layered perovskite catalysts. *Chemical*  
652 *communications* **52**, 10739-10742, doi:10.1039/c6cc04895a (2016).

- 653 26 May, K. J. *et al.* Influence of Oxygen Evolution during Water Oxidation on the  
654 Surface of Perovskite Oxide Catalysts. *The Journal of Physical Chemistry Letters* **3**,  
655 3264-3270, doi:10.1021/jz301414z (2012).
- 656 27 Risch, M. *et al.* Structural Changes of Cobalt-Based Perovskites upon Water  
657 Oxidation Investigated by EXAFS. *The Journal of Physical Chemistry C* **117**, 8628-  
658 8635, doi:10.1021/jp3126768 (2013).
- 659 28 Binninger, T. *et al.* Thermodynamic explanation of the universal correlation between  
660 oxygen evolution activity and corrosion of oxide catalysts. *Scientific reports* **5**, 12167,  
661 doi:10.1038/srep12167 (2015).
- 662 29 Grimaud, A. *et al.* Activation of surface oxygen sites on an iridium-based model  
663 catalyst for the oxygen evolution reaction. *Nature Energy* **2**, 16189,  
664 doi:10.1038/nenergy.2016.189 (2016).
- 665 30 Sen, F. G. *et al.* Towards accurate prediction of catalytic activity in IrO<sub>2</sub> nanoclusters  
666 via first principles-based variable charge force field. *J. Mater. Chem. A* **3**, 18970-  
667 18982, doi:10.1039/c5ta04678e (2015).
- 668 31 Gottesfeld, S. & Srinivasan, S. Electrochemical and optical studies of thick oxide  
669 layers on iridium and their electrocatalytic activities for the oxygen evolution reaction.  
670 *J. Electroanal. Chem. Interfacial Electrochem.* **86**, 89-104, doi:10.1016/S0022-  
671 0728(78)80358-1 (1978).
- 672 32 Reier, T., Weidinger, I., Hildebrandt, P., Kraehnert, R. & Strasser, P. Electrocatalytic  
673 oxygen evolution reaction on iridium oxide model film catalysts: influence of oxide  
674 type and catalyst substrate interactions. *ECS Trans.* **58**, 39-51, 14 pp.,  
675 doi:10.1149/05802.0039ecst (2013).
- 676 33 Pfeifer, V. *et al.* The electronic structure of iridium and its oxides. *Surface and*  
677 *Interface Analysis* **48**, 261-273, doi:10.1002/sia.5895 (2016).
- 678 34 Sanchez Casalongue, H. G. *et al.* In situ observation of surface species on iridium  
679 oxide nanoparticles during the oxygen evolution reaction. *Angewandte Chemie* **53**,  
680 7169-7172, doi:10.1002/anie.201402311 (2014).
- 681 35 Fu, W. T. & Ijdo, D. J. W. On the space group of the double perovskite Ba<sub>2</sub>PrIrO<sub>6</sub>.  
682 *Journal of Solid State Chemistry* **178**, 1312-1316, doi:10.1016/j.jssc.2005.02.003  
683 (2005).
- 684 36 Strasser, P. Free Electrons to Molecular Bonds and Back: Closing the Energetic  
685 Oxygen Reduction (ORR)-Oxygen Evolution (OER) Cycle Using Core-Shell  
686 Nanoelectrocatalysts. *Acc Chem Res* **49**, 2658-2668,  
687 doi:10.1021/acs.accounts.6b00346 (2016).
- 688 37 Minguzzi, A. *et al.* Observing the oxidation state turnover in heterogeneous iridium-  
689 based water oxidation catalysts. *Chemical Science* **5**, 3591, doi:10.1039/c4sc00975d  
690 (2014).
- 691 38 Pavlovic, Z., Ranjan, C., Gao, Q., van Gastel, M. & Schloegl, R. Probing the structure  
692 of water oxidizing anodic Iridium oxide catalyst using Raman spectroscopy. *ACS*  
693 *Catalysis*, doi:10.1021/acscatal.6b02343 (2016).
- 694 39 Cherevko, S. *et al.* Oxygen and hydrogen evolution reactions on Ru, RuO<sub>2</sub>, Ir, and  
695 IrO<sub>2</sub> thin film electrodes in acidic and alkaline electrolytes: A comparative study on  
696 activity and stability. *Catalysis Today* **262**, 170-180, doi:10.1016/j.cattod.2015.08.014  
697 (2016).
- 698 40 Trasatti, S. & Petrii, O. A. Real surface area measurements in electrochemistry. *J.*  
699 *Electroanal. Chem.* **327**, 353-376 (1992).
- 700 41 Angelinetta, C., Trasatti, S., Atanososka, L. D. & Atanasoski, R. T. Surface properties  
701 of RuO<sub>2</sub> + IrO<sub>2</sub> mixed oxide electrodes. *Journal of Electroanalytical Chemistry and*

- 702 *Interfacial Electrochemistry* **214**, 535-546, doi:[http://dx.doi.org/10.1016/0022-](http://dx.doi.org/10.1016/0022-0728(86)80122-X)  
703 [0728\(86\)80122-X](http://dx.doi.org/10.1016/0022-0728(86)80122-X) (1986).
- 704 42 Burke, L. D. & Murphy, O. J. Surface area—Voltammetric charge correlation for  
705 RuO<sub>2</sub>/TiO<sub>2</sub>-based anodes. *Journal of Electroanalytical Chemistry and Interfacial*  
706 *Electrochemistry* **112**, 39-50, doi:[http://dx.doi.org/10.1016/S0022-0728\(80\)80005-2](http://dx.doi.org/10.1016/S0022-0728(80)80005-2)  
707 (1980).
- 708 43 Burke, L. D. & Murphy, O. J. Cyclic voltammetry as a technique for determining the  
709 surface area of RuO<sub>2</sub> electrodes. *Journal of Electroanalytical Chemistry and*  
710 *Interfacial Electrochemistry* **96**, 19-27, doi:[http://dx.doi.org/10.1016/S0022-](http://dx.doi.org/10.1016/S0022-0728(79)80299-5)  
711 [0728\(79\)80299-5](http://dx.doi.org/10.1016/S0022-0728(79)80299-5) (1979).
- 712 44 Minguzzi, A. *et al.* Easy Accommodation of Different Oxidation States in Iridium  
713 Oxide Nanoparticles with Different Hydration Degree as Water Oxidation  
714 Electrocatalysts. *ACS Catalysis* **5**, 5104-5115, doi:10.1021/acscatal.5b01281 (2015).
- 715 45 Pickup, P. G. & Birss, V. I. A model for anodic hydrous oxide growth at iridium. *J.*  
716 *Electroanal. Chem. Interfacial Electrochem.* **220**, 83-100, doi:10.1016/0022-  
717 0728(87)88006-3 (1987).
- 718 46 Burke, L. D. & Whelan, D. P. A voltammetric investigation of the charge storage  
719 reactions of hydrous iridium oxide layers. *Journal of Electroanalytical Chemistry and*  
720 *Interfacial Electrochemistry* **162**, 121-141, doi:[https://doi.org/10.1016/S0022-](https://doi.org/10.1016/S0022-0728(84)80159-X)  
721 [0728\(84\)80159-X](https://doi.org/10.1016/S0022-0728(84)80159-X) (1984).
- 722 47 Fabbri, E., Haberer, A., Waltar, K., Kötz, R. & Schmidt, T. J. Developments and  
723 perspectives of oxide-based catalysts for the oxygen evolution reaction. *Catal. Sci.*  
724 *Technol.* **4**, 3800-3821, doi:10.1039/c4cy00669k (2014).
- 725 48 Reier, T., Nong, H. N., Teschner, D., Schlögl, R. & Strasser, P. Electrocatalytic  
726 Oxygen Evolution Reaction in Acidic Environments - Reaction Mechanisms and  
727 Catalysts. *Advanced Energy Materials*, 1601275, doi:10.1002/aenm.201601275  
728 (2016).
- 729 49 Rong, X., Parolin, J. & Kolpak, A. M. A Fundamental Relationship between Reaction  
730 Mechanism and Stability in Metal Oxide Catalysts for Oxygen Evolution. *ACS*  
731 *Catalysis* **6**, 1153-1158, doi:10.1021/acscatal.5b02432 (2016).
- 732 50 Grimaud, A. *et al.* Activating lattice oxygen redox reactions in metal oxides to  
733 catalyse oxygen evolution. *Nature chemistry*, doi:10.1038/nchem.2695 (2017).
- 734 51 Pfeifer, V. *et al.* Reactive oxygen species in iridium-based OER catalysts. *Chem. Sci.*,  
735 doi:10.1039/c6sc01860b (2016).
- 736 52 Pfeifer, V. *et al.* In situ observation of reactive oxygen species forming on oxygen-  
737 evolving iridium surfaces. *Chem Sci* **8**, 2143-2149, doi:10.1039/c6sc04622c (2017).
- 738 53 Pfeifer, V. *et al.* The electronic structure of iridium oxide electrodes active in water  
739 splitting. *Physical chemistry chemical physics : PCCP* **18**, 2292-2296,  
740 doi:10.1039/c5cp06997a (2016).
- 741 54 Willinger, E., Massue, C., Schlögl, R. & Willinger, M. G. Identifying Key Structural  
742 Features of IrO<sub>x</sub> Water Splitting Catalysts. *J Am Chem Soc* **139**, 12093-12101,  
743 doi:10.1021/jacs.7b07079 (2017).
- 744 55 Fierro, S., Nagel, T., Baltruschat, H. & Comninellis, C. Investigation of the oxygen  
745 evolution reaction on Ti/IrO<sub>2</sub> electrodes using isotope labelling and on-line mass  
746 spectrometry. *Electrochemistry Communications* **9**, 1969-1974,  
747 doi:10.1016/j.elecom.2007.05.008 (2007).
- 748 56 Rossmeisl, J., Qu, Z. W., Zhu, H., Kroes, G. J. & Nørskov, J. K. Electrolysis of water  
749 on oxide surfaces. *Journal of Electroanalytical Chemistry* **607**, 83-89,  
750 doi:10.1016/j.jelechem.2006.11.008 (2007).

751 57 Ooka, H., Takashima, T., Yamaguchi, A., Hayashi, T. & Nakamura, R. Element  
752 strategy of oxygen evolution electrocatalysis based on in situ spectroelectrochemistry.  
753 *Chemical communications* **53**, 7149-7161, doi:10.1039/c7cc02204b (2017).

754 58 Bockris, J. O. M. Kinetics of Activation Controlled Consecutive Electrochemical  
755 Reactions: Anodic Evolution of Oxygen. *The Journal of Chemical Physics* **24**, 817,  
756 doi:10.1063/1.1742616 (1956).

757 59 Mefford, J. T. *et al.* Water electrolysis on La(1-x)Sr(x)CoO(3-delta) perovskite  
758 electrocatalysts. *Nature communications* **7**, 11053, doi:10.1038/ncomms11053 (2016).

759 60 Cherevko, S., Geiger, S., Kasian, O., Mingers, A. & Mayrhofer, K. J. J. Oxygen  
760 evolution activity and stability of iridium in acidic media. Part 2. – Electrochemically  
761 grown hydrous iridium oxide. *Journal of Electroanalytical Chemistry* **774**, 102-110,  
762 doi:10.1016/j.jelechem.2016.05.015 (2016).

763 61 Kötz, R., Neff, H. & Stucki, S. Anodic Iridium Oxide Films; XPS-Studies of  
764 Oxidation State Changes and O<sub>2</sub>-Evolution. *J. Electrochem. Soc.* **131**, 72-77 (1984).

765 62 Kasian, O., Grote, J. P., Geiger, S., Cherevko, S. & Mayrhofer, K. J. J. The Common  
766 Intermediates of Oxygen Evolution and Dissolution Reactions during Water  
767 Electrolysis on Iridium. *Angewandte Chemie* **57**, 2488-2491,  
768 doi:10.1002/anie.201709652 (2018).

769 63 Oh, H.-S., Nong, H. N. & Strasser, P. Preparation of Mesoporous Sb-, F-, and In-  
770 Doped SnO<sub>2</sub> Bulk Powder with High Surface Area for Use as Catalyst Supports in  
771 Electrolytic Cells. *Advanced Functional Materials* **25**, 1074-1081,  
772 doi:10.1002/adfm.201401919 (2015).

773 64 Li, Z. Z., Schneegans, O. & Fruchter, L. Synthesis of Perovskite SrIrO<sub>3</sub> Thin Films by  
774 Sputtering Technique. *arXiv:1610.03722* (2016).

775 65 Klemm, S. O., Topalov, A. A., Laska, C. A. & Mayrhofer, K. J. J. Coupling of a high  
776 throughput microelectrochemical cell with online multielemental trace analysis by  
777 ICP-MS. *Electrochemistry Communications* **13**, 1533-1535,  
778 doi:10.1016/j.elecom.2011.10.017 (2011).

779 66 Grote, J. P., Zeradjanin, A. R., Cherevko, S. & Mayrhofer, K. J. Coupling of a  
780 scanning flow cell with online electrochemical mass spectrometry for screening of  
781 reaction selectivity. *The Review of scientific instruments* **85**, 104101,  
782 doi:10.1063/1.4896755 (2014).

783

784

785

786